

Oscillations excited by plasmoids formed during magnetic reconnection in a vertical gravitationally stratified current sheet

P. Jelínek¹

University of South Bohemia, Faculty of Science, Institute of Physics and Biophysics,
Branišovská 10, CZ – 370 05 České Budějovice, Czech Republic

`pjelinek@prf.jcu.cz`

M. Karlický²

Czech Academy of Sciences, v. v. i., Astronomical Institute, Fričova 258, CZ – 251 65
Ondřejov, Czech Republic

T. Van Doorselaere³

Centre for mathematical Plasma Astrophysics (CmPA), Mathematics Department, KU
Leuven, Celestijnenlaan 200B bus 2400, 3001 Leuven, Belgium

M. Bárta²

Czech Academy of Sciences, v. v. i., Astronomical Institute, Fričova 258, CZ – 251 65
Ondřejov, Czech Republic

Received _____; accepted _____

ABSTRACT

Using the FLASH code, which solves the full set of the two-dimensional (2-D) non-ideal (resistive) time-dependent magnetohydrodynamic (MHD) equations, we study processes during the magnetic reconnection in a vertical gravitationally stratified current sheet. We show that during these processes, which correspond to processes in solar flares, plasmoids are formed due to the tearing mode instability of the current sheet. These plasmoids move upwards or downwards along the vertical current sheet, and some of them merge into larger plasmoids. We study the density and temperature structure of these plasmoids and their time evolution in details. We found that during the merging of two plasmoids the resulting larger plasmoid starts to oscillate; in our model with a ~ 25 s period. On the other hand, the plasmoid moving downwards merges with the underlying flare arcade which also starts to oscillate during this process; in our model with a ~ 35 s period. It is shown that the merging process of plasmoid with the flare arcade is a complex process as presented by complex density and temperature structures of the oscillating arcade. Moreover, all these processes are associated with magnetoacoustic waves produced by the motion and merging of plasmoids.

Subject headings: Sun: corona – Sun: flares – plasmoids – waves – methods: numerical – magnetohydrodynamics (MHD)

1. Introduction

Magnetohydrodynamic (MHD) plasma waves and oscillations are omnipresent in the solar atmosphere and play a very important role in many phenomena observed in solar and stellar atmospheres (Aschwanden 2004; Stepanov et al. 2012) as well as in the problem of the acceleration of the fast component of the solar wind (e.g. Li et al. 2004; Li & Li 2008; Nakariakov et al. 2016).

The magnetically dominated solar plasma supports the propagation of various types of MHD waves (e.g. Nakariakov & Verwichte 2005; De Moortel & Nakariakov 2012; Yu et al. 2016). In solar flares, quasi-periodic pulsations (QPPs) are commonly observed in radio, soft X-ray, hard X-ray, ultraviolet, and even in gamma-ray emissions (Roberts et al. 1984; Fárník et al. 2003; Wang et al. 2005; Nakariakov et al. 2006, 2010, 2016).

The period of these oscillations ranges from sub-seconds to tens of minutes (Mészárosová et al. 2006; Tan 2008; Karlický et al. 2010b; Kupriyanova et al. 2010; Huang et al. 2014; Nisticò et al. 2014), and some of them were interpreted as manifestations of the transverse, kink mode (e.g. Kupriyanova et al. 2013) or sausage modes (e.g. Nakariakov et al. 2003), collectively supported by flare loops. When interpreted this way, the measured QPPs can be seismologically exploited to infer such key parameters as the magnetic field strength in the key region where flare energy is released (e.g. Chen et al. 2015; Guo et al. 2016; Chen et al. 2016). Several theoretical models have been proposed to explain the generation of these QPPs (Nakariakov & Melnikov 2009; Van Doorselaere et al. 2016). Quasi-periodic pulsations are often detected in almost all wavelenghts – microwave, white light, X-ray, and gamma-ray bands. The periods of QPPs are sub-second to tens of seconds. The damping time of QPPs is not yet very well measured but is around a few periods (e.g. Kolotkov et al. 2015).

Despite many theoretical models and the numerical results, it is not well understood

how QPPS are generated and the mechanisms are still debated in the literature. For the review of recent numerical results see e.g. Pascoe (2014). Here we study in detail the generation of transverse waves in a magnetic arcade impacted by plasmoids ejected from a current sheet. It deviates from the work by Takasao et al. (2015) and Takasao & Shibata (2016) in the sense that they consider a steady reconnection regime which leads to (dynamically evolving) shocks in the post-flare arcade, whereas we consider a bursty outflow from the reconnection site (in the form of plasmoids), which then excites transverse waves. Takasao & Shibata (2016) imposed a localized resistivity in their simulation model. This localized resistivity is fixed in time and space to realize a fast and quasi-steady magnetic reconnection with a single X-point. This means that they neglected the oscillations caused by plasmoids and focused on the oscillations excited by a quasi-steady reconnection outflow. Our simulation is thus complementary to their simulation because we focus just on oscillations generated during mutual interactions of plasmoids and interaction of plasmoids with the flare arcade. An excitation of the fast magnetoacoustic waves by ejected plasmoids after their interaction with ambient magnetic field was also investigated by Yang et al. (2015). However, in contrast with our present work, they performed their calculations in the so-called interchange-reconnection scenario.

Apart from the fact that the transverse waves excited by plasmoids may be the mechanism behind the observed QPPs in solar flares, they could also be important for the energy transport in solar flares. It was pointed out by Fletcher & Hudson (2008) that magnetic tension waves can play an important role in the transport of energy from the flare site to the lower atmospheric layers. The energy of the transverse waves is then transported down and dissipated in the chromosphere (Russell & Fletcher 2013; Reep & Russell 2016), where it can be used to accelerate energetic particles.

In our previous papers (Jelínek & Karlický 2012; Jelínek et al. 2012, 2015b) we

numerically investigated the behaviour of fast magnetoacoustic waves in a Harris current sheet structure but we did not consider resistivity. In the present paper we included the resistivity to show not only the formation of plasmoids and their coalescence, similarly as in the paper by Bárta et al. (2008), but also the collision of plasmoids outflowing from the reconnection site with the flare magnetic arcade, triggering oscillatory processes. It was shown previously by Innocenti et al. (2015) that Particle-In-Cell (PIC) simulations result in the formation of several plasmoids, until a large plasmoid stabilises the system.

In real flares, for a sufficiently fast reconnection process, anomalous resistivity needs to be considered. This resistivity is generated at locations where the drift of electrons, forming the electric current, overcomes some critical velocity (e.g., the ion-sound or even electron thermal velocity) (Norman & Smith 1978). In solar flare conditions it requires a very narrow current sheet (10 – 100 m). Thus, in any global MHD model of solar flares it is difficult to consider such a very narrow current sheet and simultaneously high values of the very localized anomalous resistivity. Due to this problem, in the present paper we made a compromise, we take the current sheet that is much broader than that in a real flare and the resistivity which is greater than the collisional resistivity, but lower than the anomalous one. In order to be in agreement with observed oscillations of the flare arcade and plasmoid (Veronig et al. 2006; Karlický & Kliem 2010), we have chosen the resistivity 100 times greater than the collisional one. Although in several aspects the model can be improved, it presents the processes that are new and important, and still not considered in connection with solar flares.

Tajima et al. (1987) studied the merger process of two plasmoids and they found that during this process a larger plasmoid is formed and this plasmoid oscillates with the period of about the Alfvén transit time, i.e., $P \approx L/c_A$, where L is the characteristic width of the plasmoid and c_A is the mean Alfvén speed in the plasmoid. Plasmoids in solar flares have

been observed in soft X-rays and EUV (Ohyama & Shibata 1998; Kołomański & Karlický 2007; Takasao et al. 2012; Savage et al. 2012). In some cases processes connected with these plasmoids produce the so called drifting pulsating structures (DPSs) in the decimetric range of radio waves (Kliem et al. 2000; Bárta et al. 2008, 2011; Karlický & Bárta 2011).

The paper is structured as follows: In Section 2 we present our numerical model, including the initial equilibrium and perturbations. The results of the numerical simulations and their interpretation are summarized in Section 3. Finally, we complete the paper by some conclusions in the last Sect. 4.

2. Model

2.1. Governing equations

Our numerical model describes a gravitationally stratified solar atmosphere, in which the plasma dynamics are described by the 2-D, time-dependent non-ideal (resistive) MHD equations. We use the FLASH code (Lee & Deane 2009; Lee 2013), where the MHD equations are formulated in conservative form as

$$\frac{\partial \varrho}{\partial t} + \nabla \cdot (\varrho \mathbf{v}) = 0, \quad (1)$$

$$\frac{\partial \varrho \mathbf{v}}{\partial t} + \nabla \cdot (\varrho \mathbf{v} \mathbf{v} - \mathbf{B} \mathbf{B}) + \nabla p_* = \varrho \mathbf{g}, \quad (2)$$

$$\begin{aligned} \frac{\partial \varrho E}{\partial t} + \nabla \cdot [(\varrho E + p_*) \mathbf{v} - \mathbf{B}(\mathbf{v} \cdot \mathbf{B})] = \\ = \varrho \mathbf{g} \cdot \mathbf{v} + \nabla \cdot (\mathbf{B} \times (\eta \nabla \times \mathbf{B})), \end{aligned} \quad (3)$$

$$\frac{\partial \mathbf{B}}{\partial t} + \nabla \cdot (\mathbf{v} \mathbf{B} - \mathbf{B} \mathbf{v}) = -\nabla \times (\eta \nabla \times \mathbf{B}), \quad (4)$$

$$\nabla \cdot \mathbf{B} = 0. \quad (5)$$

Here ρ is the mass density, \mathbf{v} is the flow velocity, \mathbf{B} is the magnetic field strength, $\mathbf{g} = [0, -g_{\odot}, 0]$ is the gravitational acceleration with $g_{\odot} = 274 \text{ ms}^{-2}$ and η is the magnetic diffusivity. According to Priest (1982), the magnetic diffusivity in the collisional regime can be expressed as $\eta = 10^9 T^{-3/2}$, which gives us for the temperature $T \approx 10^6 \text{ K}$ a value $1 \text{ m}^2 \cdot \text{s}^{-1}$. To see the magnetic reconnection in our models at reasonable times, we tested different values of the magnetic diffusivity and finally used the value which is 100 times higher than the collisional diffusivity, but much smaller than the anomalous one. The total pressure p_* is given by:

$$p_* = \left(p + \frac{B^2}{2\mu_0} \right), \quad (6)$$

p is the fluid thermal pressure, B is the magnitude of the magnetic field. The specific total energy E in Eq. (3) is expressed as:

$$E = \epsilon + \frac{v^2}{2} + \frac{B^2}{2\mu_0\rho}, \quad (7)$$

where ϵ is the specific internal energy:

$$\epsilon = \frac{p}{(\gamma - 1)\rho}, \quad (8)$$

with the adiabatic coefficient $\gamma = 5/3$, v is the magnitude of the flow velocity and $\mu_0 = 1.26 \times 10^{-6} \text{ Hm}^{-1}$ is the magnetic permeability of free space.

Generally, the terms expressing the radiative losses R_{loss} , thermal conduction T_{cond} and heating H should be added to the set of MHD equations. In the initial state it is assumed that the radiative losses and thermal conduction are fully compensated by the heating H , i.e., $R_{\text{loss}} + T_{\text{cond}} + H = 0$, otherwise the unperturbed atmosphere is not in equilibrium, e.g., due to the steep temperature gradient in the transition region. Problems appear when the atmosphere is perturbed. Namely, there is no simple expression for the heating term H , which in the unperturbed atmosphere fully compensates R_{loss} and T_{cond} , and in the perturbed atmosphere correctly describes the heating. Therefore, for the purpose of our study, we assume that $R_{\text{loss}} + T_{\text{cond}} + H = 0$ is valid during the whole studied processes.

2.2. Initial equilibrium

For a static ($\mathbf{v} = \mathbf{0}$) equilibrium, the Lorentz and gravity forces must be balanced by the pressure gradient in the entire physical domain

$$-\nabla p + \mathbf{j} \times \mathbf{B} + \varrho \mathbf{g} = \mathbf{0}. \quad (9)$$

The solenoidal condition, $\nabla \cdot \mathbf{B} = 0$, is identically satisfied by using a magnetic flux function, \mathbf{A} ,

$$\mathbf{B} = \nabla \times \mathbf{A}. \quad (10)$$

For calculating the magnetic field in the vertically oriented current sheet, we use the magnetic flux function $\mathbf{A} = [0, 0, A_z]$ as e.g. Jelínek et al. (2012, 2015b)

$$A_z = -B_0 w_{\text{cs}} \ln \left\{ \left| \cosh \left(\frac{x}{w_{\text{cs}}} \right) \right| \right\} \exp \left(-\frac{y}{\lambda} \right). \quad (11)$$

Here the coefficient $\lambda \approx 100$ Mm denotes the magnetic scale-height. The symbol B_0 is used for the external magnetic field and w_{cs} is the half width of the current-sheet. We set $w_{\text{cs}} = 0.15$ Mm. Note, that the prescription for \mathbf{g} and \mathbf{A} implies a current-sheet in the vertical direction y with the current density flowing in the invariant direction z ; x being the horizontal direction perpendicular to the current-sheet.

The equilibrium gas pressure and mass density are computed according to the following equations, see e.g. Solov'ev (2010) and Jelínek et al. (2015a):

$$p(x, y) = p_{\text{h}}(y) - \frac{1}{\mu_0} \left[\int_{-\infty}^x \frac{\partial^2 A}{\partial y^2} \frac{\partial A}{\partial x} dx + \frac{1}{2} \left(\frac{\partial A}{\partial x} \right)^2 \right], \quad (12)$$

$$\begin{aligned} \varrho(x, y) &= \varrho_{\text{h}}(y) + \frac{1}{\mu_0 g_{\odot}} \left\{ \frac{\partial}{\partial y} \left[\int_{-\infty}^x \frac{\partial^2 A}{\partial y^2} \frac{\partial A}{\partial x} dx + \right. \right. \\ &\quad \left. \left. + \frac{1}{2} \left(\frac{\partial A}{\partial x} \right)^2 \right] - \frac{\partial A}{\partial y} \nabla^2 A \right\}. \end{aligned} \quad (13)$$

With the use of Eq. (11) in these general formulas we obtain the expressions for the equilibrium gas pressure

$$p(x, y) = p_h(y) - \frac{B_0^2}{2\mu_0} \left\{ \frac{w_{\text{cs}}^2}{\lambda^2} \ln^2 \left[\cosh \left(\frac{x}{w_{\text{cs}}} \right) \right] + \tanh^2 \left(\frac{x}{w_{\text{cs}}} \right) \right\} \exp \left(-\frac{2y}{\lambda} \right), \quad (14)$$

and mass density

$$\varrho(x, y) = \varrho_h(y) - \frac{B_0^2}{\mu_0 g_\odot \lambda} \left\{ \tanh^2 \left(\frac{x}{w_{\text{cs}}} \right) - \ln \left[\cosh \left(\frac{x}{w_{\text{cs}}} \right) \right] \operatorname{sech}^2 \left(\frac{x}{w_{\text{cs}}} \right) \right\} \exp \left(-\frac{2y}{\lambda} \right), \quad (15)$$

where

$$p_h(y) = p_0 \exp \left[-\int_{y_0}^y \frac{1}{\Lambda(\tilde{y})} d\tilde{y} \right], \quad (16)$$

and

$$\varrho_h(y) = \frac{p(y)}{g_\odot \Lambda(y)}. \quad (17)$$

Here

$$\Lambda(y) = \frac{k_{\text{B}} T(y)}{\bar{m} g_\odot} \quad (18)$$

is the pressure scale-height which in the case of isothermal atmosphere represents the vertical distance over which the gas pressure decreases by a factor of $e \approx 2.7$, $k_{\text{B}} = 1.38 \times 10^{-23} \text{ J} \cdot \text{K}^{-1}$ is the Boltzmann constant and $\bar{m} = 0.6 m_{\text{p}}$ is the mean particle mass ($m_{\text{p}} = 1.672 \times 10^{-27} \text{ kg}$ is the proton mass). p_0 in Eq. (16) denotes the gas pressure at the reference level y_0 . In our calculations we set $y_0 = 10 \text{ Mm}$.

For the solar atmosphere, the temperature profile $T(y)$, was derived by Vernazza et al. (1981); Avrett & Loeser (2008). At the top of the photosphere, which corresponds to the height of $y = 0.5 \text{ Mm}$, the temperature is $T(y) = 5700 \text{ K}$. At higher altitudes, the

temperature falls down to its minimal value $T(y) = 4350$ K at $y \approx 0.95$ Mm. Higher up the temperature rises slowly to the height of about $y = 2.7$ Mm, where the transition region (TR) is located. Here the temperature increases abruptly to the value $T(y) = 1.5$ MK, at the altitude $y = 10$ Mm, which is typical for the solar corona.

2.3. Perturbations

At the beginning of the numerical simulation ($t = 0$ s), the equilibrium is perturbed by a Gaussian compression pulse in the x -component of velocity and has the following form (e.g. Nakariakov et al. 2004, 2005):

$$v_x = -A_0 \frac{x}{\lambda_x} \exp \left[- \left(\frac{x}{\lambda_x} \right)^2 \right] \exp \left[- \left(\frac{y - L_P}{\lambda_y} \right)^2 \right], \quad (19)$$

where $A_0 = 1 \text{ km} \cdot \text{s}^{-1}$ is the initial amplitude of the pulse, and $\lambda_x = \lambda_y = 0.15$ Mm are the widths of the velocity pulse in the longitudinal and transverse directions, respectively. For such an initial velocity pulse, the ratio between the maximum of kinetic energy density and the background (thermal) energy density is $\approx 4.167 \times 10^{-5}$. The perturbation point ($x = 0, y = L_P$) is located on the axis of the current-sheet, at a distance of $L = 25$ Mm from the bottom boundary of the simulation region. This pulse is used in order to start the primary tearing instability in the current-sheet. Later on, because of the resistivity used in our model, a number of plasmoids as well as the magnetic arcade in the bottom part of the simulation region is formed self-consistently.

3. Numerical solutions and results

We solve the 2-D time-dependent, ideal MHD equations (1)-(4) numerically, making use of the FLASH code (Lee & Deane 2009; Lee 2013). It is a well tested, fully modular,

parallel, multi-physics, open science, simulation code that implements second- and third-order unsplit Godunov solvers with various slope limiters and Riemann solvers as well as adaptive mesh refinement (AMR, e.g. Chung 2002). The Godunov solver combines the corner transport upwind method for multi-dimensional integration and the constrained transport algorithm for preserving the divergence free constraint on the magnetic field (Lee & Deane 2009). We use the minmod slope limiter and the Riemann solver (e.g. Toro 2006). The main advantage of using the AMR technique is to refine a numerical grid at steep spatial profiles while keeping the grid coarse at the places where fine spatial resolution is not essential. In our case, the AMR strategy is based on controlling the numerical errors near the gradient of mass density, leading to a reduction of the numerical diffusion within the entire simulation region.

For our numerical simulations, we use a 2-D Eulerian box of height $H = 100$ Mm and width $W = 20$ Mm. The spatial resolution of the numerical grid is determined with the AMR method and we use a similar setup as in the case of the vertical current-sheet presented in Jelínek et al. (2015b). We use an AMR grid with the minimum (maximum) level of the refinement blocks set to 3(6) to have 203 328 numerical cells (Fig. 1).

Prior to performing the numerical simulations, we verified that the system remains in numerical equilibrium for the adopted grid resolution, by running a test simulation without any velocity pulse.

Very shortly after the initial pulse, the magnetic field reconnects and plasmoids (2-D O-type magnetic field structures) are generated. The plasmoids move up and down in the current sheet, exciting oscillations in the plasmoids themselves and the magnetic arcade. These processes are described in the following subsections. For better visibility of oscillations and other processes we also enclosed the movie from our numerical simulations.

3.1. Plasmoid merging and oscillations

In Fig. 2, we show the mass density and magnetic field lines for times 80, 90, 100 and 110 s, respectively. After the beginning of the magnetic reconnection, a number of plasmoids are formed in the vertical current sheet due to the tearing mode instability. During the simulation, some plasmoids merge into bigger ones and move upwards through the corona and downwards to the solar photosphere, because of the gravitational or buoyancy forces. At time $t = 80$ s and in the $y = 20 - 50$ Mm interval (Fig. 2, first panel), there are two plasmoids which move towards each other. Around time $t = 90$ s (Fig. 2, second panel), they start to merge into one larger plasmoid which then oscillates. These oscillations are clearly visible at times 100 and 110 s. At that time, the oscillating plasmoid inverts its sense of propagation direction and starts to move up, see the enclosed movie. At the time around 160 s, the oscillations are almost completely damped and the plasmoid slowly increases its size (in height 70 – 80 Mm) and at time around 200 s leaves freely the simulation region, as can also be seen in the movie.

Fig. 3 provides a zoom-in for a detailed look at the behaviour of the oscillating plasmoid and its inner structure for times 90, 100, 110 and 120 s. The blue and red dashed lines correspond to a 1D density slice for both, a vertical direction and a horizontal direction, respectively. The positions of slices are chosen on the axis of symmetry of simulation region ($x = 0.0$ Mm), panels marked as (a), and at the place, where we found the maximum of mass density on this axis, panels marked as (b) – ($\approx 32 - 33$ Mm), respectively – see Fig. 4. Two peaks in graphs (a) for times 80 – 100 s represent two plasmoids which move towards each other and merge into one plasmoid which is finally represented by an increase of mass density in one peak visible at time 110 s. In all displayed panels (b) we can recognize very nicely the complex internal plasmoid structure shortly before and after the merging process.

Figure 5 shows the interaction of the two plasmoids followed by oscillations of the

merged larger plasmoid. Essentially, the figure shows the temporal map of the vector potential at heights between 18 – 50 Mm. To show clearly the plasmoids and their merging in this color map we use only the selected values of the vector potential corresponding to their magnetic field lines. Here, we can see very clearly the plasmoid motion into higher altitudes of the solar atmosphere at times after 125 s. The plasmoid (P_1) and plasmoid (P_2) are determined by two magnetic field lines (black solid lines) on the current sheet axis determined by the vector potentials $A = -2.45$ and $A = -4.9$. P indicates the resulting plasmoid which starts to oscillate with a $\tau_{\text{plas}} \approx 25$ s period, after the merger from the two plasmoids (P_1) and (P_2). This period is very close to that one calculated from the formula $\tau_{\text{plas}} = L/c_A = 27.9$ s, where $L \approx 6$ Mm is the size of plasmoid and $c_A \approx 0.215$ Mm \cdot s $^{-1}$ is the Alfvén speed in the lateral parts of the plasmoid (Tajima et al. 1987).

To show clearly the oscillatory process in the newly formed bigger plasmoid we present Fig. 6. Here we can see the temporal evolution of the maximum of the mass density on the axis of current sheet between the heights 25 – 42 Mm, where a clear oscillatory behaviour of this plasmoid is observed. We can see here a wavy signal with an initial rarefaction around the time ≈ 90 s followed by a compression at time ≈ 95 s. This initial phase continues with the next two oscillations which are very quickly attenuated, so that at time ≈ 160 s they are damped entirely. Firstly, we checked if this strong damping of oscillations is caused by the magnetic diffusivity. But, the diffusion time calculated as $\tau_{\text{damp}} \approx \mathcal{L}^2/\eta = 2.5 \times 10^9$ s, see (Roberts 1967), where $\mathcal{L} \approx 5$ Mm is the plasmoid width and the assumed magnetic diffusivity $\eta \approx 100$ m 2 \cdot s $^{-1}$, is very long. Secondly, we performed a calculation with twice higher spatial resolution and find that the damping time essentially was not changed. Furthermore, we made a special MHD test with a simple oscillating slab and we varied the resistivity in the interval from zero up to the resistivity, which is 100 times greater than the collisional resistivity (the resistivity used in this paper). In this test, in the mentioned interval of the resistivity, no change of the damping was found. Therefore,

we made a detailed analysis and we found that the plasmoid is not an isolated oscillating system, it is strongly coupled with plasma flows in its vicinity, and the damping (decrease of the oscillation amplitude) is caused by these mass plasma flows, see the enclosed movie, showing the plasma velocity field.

3.2. Arcade oscillations

Fig. 7 shows the mass density and magnetic field lines, for the times during the collision of the plasmoid with the magnetic arcade. At time $t = 120$ s and for y below 20 Mm (Fig. 7, first panel), the plasmoid moves downwards to the magnetic arcade because of the gravitational force and tension of the surrounding magnetic field lines. Shortly after, at time $t = 130$ s (Fig. 7, second panel), the plasmoid and arcade merge into one bigger arcade which starts to oscillate, as can be seen at times $t = 140$ and 150 s (Fig. 7, third and last panel), see also the enclosed movie. From our numerical simulations we found that the arcade oscillations are also very quickly damped. The reason for this damping is exactly the same as in the case of plasmoids oscillations. The arcade is not an isolated system, it is strongly coupled with processes in the current sheet. The downward oriented plasma flow, carrying plasmoids from reconnection towards the arcade, not only triggers the arcade oscillation, but in the following times the mass plasma flow damps this arcade oscillation, see the enclosed movie.

In Fig. 8 we show in detail the densities during the coalescence process, again together with the vertical (blue dashed line) and horizontal (red dashed line) slices. In Fig. 9 we present the slices, which are, similarly as in Fig. 4, in the positions of the axis of symmetry ($x = 0.0$ Mm) and the position where we find the maximum of mass density on this axis, i.e. $y \approx 7 - 9$ Mm. In panel (a) for time 125 s the hump in mass density represents the plasmoid moving downwards to the magnetic arcade, see the movie. At time 135 s we

observe the newly formed arcade which starts to oscillate, see the moving humps in panels (a) for times 155 and 175 s (compare with the temperature in Fig. 13). Contrary to panels (b) displayed in Fig. 4, the mass density in the center of the current sheet is lower than in the surrounding plasma. This is caused by the fact that the plasmoid is more dense than the plasma in the place where it was formed. But, because of the gravitational, downward acceleration of the plasma jet, the plasmoid moves down to lower altitudes of the solar atmosphere (transition region), where the density is higher, thus reversing the density contrast.

In Figs. 10 and 11 we present again the temporal maps of the vector potential at heights 2 – 18 Mm above the solar surface. Similar to Fig. 5, we draw selected vector potentials (magnetic field lines), showing clearly the oscillations of the top of the arcade.

Figure 10 shows a descent of the arcade top (determined by the magnetic field line in the current sheet axis with the vector potential $A = -2.7$ and $A = -3.5$) at the early stage of the magnetic field reconnection (50 – 80 s) in the vertical and gravitationally stratified current sheet. This process was already proposed to explain the downward motion of the X-ray source at the beginning of the 3 November 2003 flare (Veronig et al. 2006).

Figure 11 shows the interaction of the plasmoid with the arcade and clearly shows the subsequent arcade oscillations. The plasmoid (P) and arcade (A) are determined by two magnetic field lines at the current sheet axis with the vector potential $A = -3.2$ and $A = -4.9$. As seen here, after the interaction of the plasmoid with the arcade, the arcade starts to oscillate with a 35 s period. Moreover, it can be seen that oscillations of different layers of the arcade are not fully synchronized, as is evidenced by the phase lag between the maxima of the arcade oscillations expressed by the lines with $A = -3.2$ and $A = -4.9$.

In Fig. 12, we present the temporal evolution of the y component of the velocity $-v_y$ in seven detection points along the selected magnetic field line with the vector-potential

$A = -3.9$. On the left panel of Fig. 12, we show the signals from the left side of the arcade and on the right panel signals from the right side of the arcade. The colours correspond to the positions (depending on the side of symmetry – left or right) as follows: black (0.0 Mm), blue (-0.3125 Mm; 0.3125 Mm), green (-0.625 Mm; 0.625 Mm) and red (-0.9375 Mm; 0.9375 Mm), respectively. As can be seen here, the oscillations are synchronized at both sides of the arcade and quickly damped. Here, similarly as in the case of the damping of the oscillating plasmoid, we think that this damping is caused by a strong coupling between the oscillating flare arcade and plasma outflows from the above located magnetic reconnection. We estimate the period of the wave signal as $\tau_{\text{arc}} \approx 35$ s. Here as well, the estimated wave period corresponds to the formula $\tau_{\text{arc}} = L/c_A = 38.9$ s, where L is a length of the loop and c_A is average Alfvén speed in the loop. A very important finding from our numerical simulation of the collision of a plasmoid and a magnetic arcade is that the impinging plasmoid can excite a transverse wave in the arcade as seen from both parts of Fig. 12. We can infer that standing waves are observed in our simulations because the peaks of the wave signal are synchronized very well between symmetric locations, as seen in Fig. 12. These standing, transverse waves may be responsible for the generation of the observed QPPs in solar flares.

To complete this part of our study, we show the time evolution of the temperature for different times 125, 135, 155 and 175 s in Fig. 13. We shifted the bottom boundary to higher altitudes of the solar atmosphere (4 Mm) because of better readability in a linear temperature scale. We can clearly see that the plasmoid coalescence causes a temperature enhancement up to ≈ 80 MK. Note, that in real flares, especially in high-temperature regions there are deviations from our simplifying assumption ($R_{\text{loss}} + T_{\text{cond}} + H = 0$), and thus we expect that the real temperature will be lower. This temperature blob moves slowly down and after the collision and merging of the plasmoid with the arcade this blob starts to oscillate following the position of the top of the newly created magnetic arcade. During the

observed oscillations, there is practically no change of the maximum of the temperature, so it remains almost at the same value.

Using relations according to Aschwanden (2004) we estimated the radiative cooling times τ_R (in optically thin approximation) and conductive cooling times τ_C (parallel to the magnetic field lines) in several selected positions at the time 175 s (the time with the maximal temperature in the arcade top source). We found that at this instant the radiative cooling time for the plasmoid is $\tau_R \approx 19$ s, for the arcade top source is $\tau_R \approx 15$ s and for the upper chromosphere $\tau_R \approx 0.3$ s. On the other hand, the conductive cooling times in the parallel direction to the magnetic field lines for the arcade top source is $\tau_C \approx 0.025$ s and for the transition region $\tau_C \approx 12$ s. The conductive cooling times in the perpendicular direction to the magnetic field lines are typically several orders longer. As can be seen, the shortest times are the conductive cooling time at the hot arcade top (extreme in the present computation) and the radiative cooling time at the upper chromosphere. It looks that the temperature inside the arcade will be in very short time smoothed and the upper chromosphere will rapidly cool to a very low temperature. But in reality, there is an additional heating, which is not well known and keeps for example the chromosphere and the transition region stable for long time. For this reason we used the assumption that the radiative and conductive losses are compensated by the assumed additional heating. This is a weak aspect of our simulations, especially for the hot arcade top. But, to add the terms for radiative and conductive losses to MHD equations without the additional heating term does not solve the problem according to our opinion. We found a hot source in the flare arcade top, as observed, but its temperature is much higher than that in observed loop-top sources. In this case, we think that our assumption about compensation of radiative and conductive losses is not valid.

The high temperature near the loop top may result in associated loop-top sources of

flares. Therefore, the current mechanism of a merging plasmoid with a magnetic arcade could compete with, operate simultaneously, or help the previously proposed mechanism of Fang et al. (2016). They proposed that the inverse Compton scattering together with Kelvin-Helmholtz turbulence could lead to long-lived loop-top sources.

As for the energetic aspects of the merging, the kinetic, potential and magnetic energy of the plasmoid is completely absorbed in the arcade, because there is no reflected plasmoid in Fig. 12 (bottom right panel). Thus, the plasmoids may form the missing link for energy transport in flares. The plasmoids could be the agent transporting a large part of the energy from the flare site to the arcade. From there, the waves in the arcade may take over the energy transport. After coalescence with the underlying magnetic arcade, the plasmoid energy is now stored and transported in the arcade in the form of fast or Alfvén waves, following the scenario outlined by Fletcher & Hudson (2008). This energy is then dissipated in the lower atmospheric layers by non-ideal effects (see, e.g. Reep & Russell 2016). Such a scenario is a hybrid between previously proposed energy transport mechanisms in flares.

4. Conclusions

We numerically studied the oscillatory and wave processes in a gravitationally stratified current sheet, together with a realistic solar atmosphere structured as the VAL-C model, using the 2D time-dependent non-ideal (resistive) MHD equations solved by the FLASH numerical code, which implements AMR.

We can summarize our results as follows. We generated an initial gaussian pulse with the horizontal component of the velocity in the current sheet, which triggers the primary reconnection. Subsequently it leads to the formation of a number of plasmoids. These plasmoids, under the gravitational and buoyancy forces start to move upwards or

downwards. After some time, the formed plasmoids collide with each other as well as with the magnetic arcade formed in the lower altitudes of the solar atmosphere. We found that the magnetic arcade shrinks in the very early phases of evolution, in agreement with observations of downward motion of the X ray source at the beginning of the 3 November 2003 flare (Veronig et al. 2006).

As a consequence of the plasmoid collisions, they form very easily much bigger plasmoids which oscillate. We observed in our simulation such a plasmoid with an oscillation period of ≈ 25 s. This period is compatible with the calculated Alfvén travel time within the plasmoid. In line with the simulations made by Kliem et al. (2000); Karlický & Bárta (2007); Karlický et al. (2010a), we expect that this oscillation process can generate the drifting pulsating structure (DPS) with a "wavy" appearance on the radio spectrum (Karlický et al. 2016).

Moreover, for the first time, we have shown that plasmoids impacting a magnetic arcade can efficiently generate transverse waves. The vertically polarised transverse waves have a period of 35 s, which is once again compatible with Alfvén travel times in the arcade. The excitation of these transverse waves could be very important for explaining QPPs and energy propagation in a solar flare. We propose that plasmoids may carry away part of the energy from the reconnection site, which is consequently efficiently deposited in the underlying arcade, leading to wave dissipation in the (non-ideal) lower layers.

In our simulations we use the simplified assumption that the radiative and conductive losses are compensated by the heating. This assumption is correct in the initial equilibrium flare atmosphere. In the perturbed atmosphere, deviations from this assumption certainly exist, especially in the very hot source at the arcade top. However, oscillations of the plasmoid and arcade found in the present computations are very similar to those observed. For example, see Figure 5 and 6 in the paper by Karlický & Kliem (2010), where the

plasmoid and its oscillation in the brightness temperature and area are shown. The period of this oscillation was about 40 s. On the other hand, in Figure 6 (panel c) in the paper by Veronig et al. (2006) it can be seen that the velocity of the X-ray loop-top source shows a damped oscillation at the very beginning of the flare. Thus, these observations can be considered as supporting our results.

The oscillations of the arcade and plasmoid were strongly damped. Analyzing this process we found that the oscillating plasmoid as well as the oscillating arcade are not isolated oscillating systems. Both are strongly coupled with processes in the vertical current sheet through plasma flows. The downward oriented plasma flow, carrying plasmoids from the reconnection towards the arcade, not only triggers the arcade oscillations, but the flow damps this arcade oscillation subsequently. Similarly, the plasma flows in the vicinity of the oscillating plasmoid damp its oscillation.

Finally, we found that in both processes (merging of two plasmoids and interaction of a plasmoid with a flare arcade) the internal structure of the plasmoids as well as the arcades is very complex. Even an oscillating region with a very hot plasma close to the arcade top was generated. However, for a more realistic description of these hot plasma regions the radiative and conductive losses need to be included into simulations, which constitutes future work. Furthermore, we will additionally add numerical resolution in the arcade regions, to allow for a better characterisation of the wave nature.

In our numerical simulations, we use a constant resistivity over the entire simulation region. For this reason, we have plasmoids and a magnetic arcade of comparable sizes and as a consequence of their collision standing waves are triggered. It may be that smaller plasmoids impacting on larger arcades would rather excite propagating, transverse waves. This could also be the subject of future research.

The authors thank the referee for constructive comments that improved the paper. P. J., M. B. and M. K. acknowledge support from Grants 16-13277S and 17-16447S of the Grant Agency of the Czech Republic. T. V. D. was supported by an Odysseus grant of the FWO Vlaanderen, the IAP P7/08 CHARM (Belspo) and the GOA-2015-014 (KU Leuven). The results were inspired by discussions at the ISSI Bern and at ISSI Beijing. The authors also express their thanks to Prof. Kris Murawski for valuable discussions. The FLASH code used in this work was developed by the DOE-supported ASC/Alliances Center for Astrophysical Thermonuclear Flashes at the University of Chicago.

REFERENCES

- Aschwanden, M. J. 2004, *Physics of the Solar Corona. An Introduction* (Praxis Publishing Ltd)
- Avrett, E. H. & Loeser, R. 2008, *ApJS*, 175, 229
- Bárta, M., Büchner, J., Karlický, M., & Skála, J. 2011, *ApJ*, 737, 24
- Bárta, M., Vršnak, B., & Karlický, M. 2008, *A&A*, 477, 649
- Chen, S.-X., Li, B., Xiong, M., Yu, H., & Guo, M.-Z. 2015, *ApJ*, 812, 22
- Chen, S.-X., Li, B., Xiong, M., Yu, H., & Guo, M.-Z. 2016, *ApJ*, 833, 114
- Chung, T. J. 2002, *Computational Fluid Dynamics*, 1036
- De Moortel, I. & Nakariakov, V. M. 2012, *Philosophical Transactions of the Royal Society of London Series A*, 370, 3193
- Fang, X., Yuan, D., Xia, C., Van Doorselaere, T., & Keppens, R. 2016, *ApJ*, 833, 36
- Farge, M. 1992, *Annual Review of Fluid Mechanics*, 24, 395
- Fárník, F., Karlický, M., & Švestka, Z. 2003, *Sol. Phys.*, 218, 183
- Fletcher, L. & Hudson, H. S. 2008, *ApJ*, 675, 1645
- Fryxell, B., Olson, K., Ricker, P., et al. 2000, *ApJS*, 131, 273
- Goedbloed, J. P. H. & Poedts, S. 2004, *Principles of Magnetohydrodynamics*
- Guo, M.-Z., Chen, S.-X., Li, B., Xia, L.-D., & Yu, H. 2016, *Sol. Phys.*, 291, 877
- Huang, J., Tan, B., Zhang, Y., Karlický, M., & Mészárosová, H. 2014, *ApJ*, 791, 44

- Innocenti, M. E., Goldman, M., Newman, D., Markidis, S., & Lapenta, G. 2015, *ApJ*, 810, L19
- Jelínek, P. & Karlický, M. 2012, *A&A*, 537, A46
- Jelínek, P., Karlický, M., & Murawski, K. 2012, *A&A*, 546, A49
- Jelínek, P., Karlický, M., & Murawski, K. 2015a, *ApJ*, 812, 105
- Jelínek, P., Srivastava, A. K., Murawski, K., Kayshap, P., & Dwivedi, B. N. 2015b, *A&A*, 581, A131
- Jiříčka, K. & Karlický, M. 2008, *Sol. Phys.*, 253, 95
- Karlický, M. & Bárta, M. 2007, *A&A*, 464, 735
- Karlický, M. & Bárta, M. 2011, *ApJ*, 733, 107
- Karlický, M., Bárta, M., & Rybák, J. 2010a, *A&A*, 514, A28
- Karlický, M., Fárník, F., & Krucker, S. 2004, *A&A*, 419, 365
- Karlický, M. & Kliem, B. 2010, *Sol. Phys.*, 266, 71
- Karlický, M., Zlobec, P., & Mészárosová, H. 2010b, *Sol. Phys.*, 261, 281
- Karlický, M. and Jiříčka, K. & Bárta, M. 2016, *Central European Astrophysical Bulletin*, 40, 93
- Kliem, B., Karlický, M., & Benz, A. O. 2000, *A&A*, 360, 715
- Kołomański, S. & Karlický, M. 2007, *A&A*, 475, 685
- Kolotkov, D. Y., Nakariakov, V. M., Kupriyanova, E. G., Ratcliffe, H., & Shibasaki, K. 2015, *A&A*, 574, A53

- Kupriyanova, E. G., Melnikov, V. F., Nakariakov, V. M., & Shibasaki, K. 2010, *Sol. Phys.*, 267, 329
- Kupriyanova, E. G., Melnikov, V. F., & Shibasaki, K. 2013, *Sol. Phys.*, 284, 559
- Lee, D. 2013, *Journal of Computational Physics*, 243, 269
- Lee, D. & Deane, A. E. 2009, *Journal of Computational Physics*, 228, 952
- Li, B., Li, X., Hu, Y.-Q., & Habbal, S. R. 2004, *Journal of Geophysical Research (Space Physics)*, 109, A07103
- Li, B. & Li, X. 2008, *ApJ*, 682, 667
- Mészárosová, H., Karlický, M., Rybák, J., Fárník, F., & Jiříčka, K. 2006, *A&A*, 460, 865
- Nakariakov, V. M., Melnikov, V. F., & Reznikova, V. E. 2003, *A&A*, 412, L7
- Nakariakov, V. M., Arber, T. D., Ault, C. E., et al. 2004, *MNRAS*, 349, 705
- Nakariakov, V. M., Foullon, C., Verwichte, E., & Young, N. P. 2006, *A&A*, 452, 343
- Nakariakov, V. M., Inglis, A. R., Zimovets, I. V., et al. 2010, *Plasma Physics and Controlled Fusion*, 52, 124009
- Nakariakov, V. M. & Melnikov, V. F. 2009, *Space Sci. Rev.*, 149, 119
- Nakariakov, V. M., Pascoe, D. J., & Arber, T. D. 2005, *Space Sci. Rev.*, 121, 115
- Nakariakov, V. M., Pilipenko, V., Heilig, B., et al. 2016, *Space Sci. Rev.*, 200, 75
- Nakariakov, V. M. & Verwichte, E. 2005, *Living Reviews in Solar Physics*, 2
- Nisticò, G., Pascoe, D. J., & Nakariakov, V. M. 2014, *A&A*, 569, A12
- Norman, C. A. & Smith, R. A. 1978, *A&A*, 68, 145

- Ohyama, M. & Shibata, K., 1998, *ApJ*, 499, 934
- Pascoe, D. J. 2014, *Research in Astronomy and Astrophysics*, 14, 805
- Priest, E. R. 1982, *Solar magneto-hydrodynamics*, D. Reidel, Holland, p. 195
- Reep, J. W. & Russell, A. J. B. 2016, *ApJ*, 818, L20
- Roberts, P. H. 1967, *An Introduction to Magnetohydrodynamics*, by P. H. Roberts. Textbook published by Longmans, Green and Co ltd, London, 1967
- Roberts, B., Edwin, P. M., & Benz, A. O. 1984, *ApJ*, 279, 857
- Russell, A. J. B. & Fletcher, L. 2013, *ApJ*, 765, 81
- Savage, S. L., Holman, G., Reeves, K. K., et al. 2012, *ApJ*, 754, 13
- Solov'ev, A. A. 2010, *Astronomy Reports*, 54, 86
- Stepanov, A. V., Zaitsev, V. V., & Nakariakov, V. M. 2012, *Coronal Seismology: Waves and Oscillations in Stellar Coronae Flare Plasma*
- Tajima, T., Sakai, J., Nakajima, H., et al. 1987, *ApJ*, 321, 1031
- Takasao, S., Asai, A., Isobe, H., & Shibata, K. 2012, *ApJ*, 745, L6
- Takasao, S., Matsumoto, T., Nakamura, N., & Shibata, K. 2015, *ApJ*, 805, 135
- Takasao, S. & Shibata, K. 2016, *ApJ*, 823, 150
- Tan, B. 2008, *Sol. Phys.*, 253, 117
- Toro, E. F. 2006, *International Journal for Numerical Methods in Fluids*, 52, 433
- Torrence, C. & Compo, G. P. 1998, *Bulletin of the American Meteorological Society*, 79, 61

Van Doorselaere, T., Kupriyanova, E. G., & Yuan, D. 2016, *Sol. Phys.*, 291, 3143

Vernazza, J. E., Avrett, E. H., & Loeser, R. 1981, *ApJS*, 45, 635

Veronig, A. M., Karlický, M., Vršnak, B., et al. 2006, *A&A*, 446, 675

Wang, T. J., Solanki, S. K., Innes, D. E., & Curdt, W. 2005, *A&A*, 435, 753

Yang, L., Zhang, L., He, J., et al. 2015, *ApJ*, 800, 111

Yu, H., Li, B., Chen, S.-X., Xiong, M., & Guo, M.-Z. 2016, *ApJ*, 833, 51

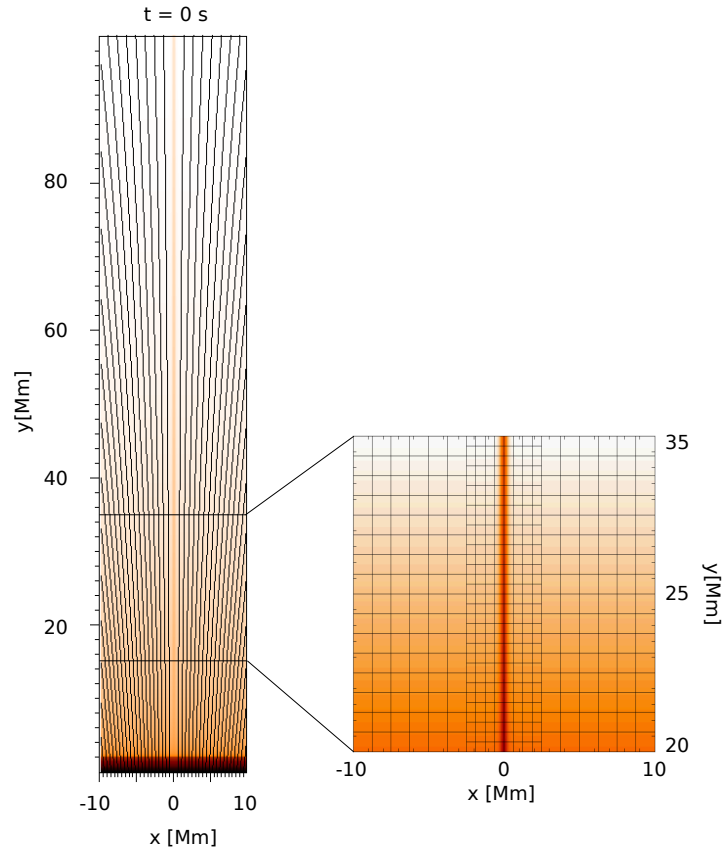


Fig. 1.— Left: Initial mass density distribution over-plotted by the magnetic field structure as black lines. Right: The detail of the simulation region in the vicinity of perturbation point (25 Mm), illustrating the computational grid, with adaptive mesh refinement (AMR).

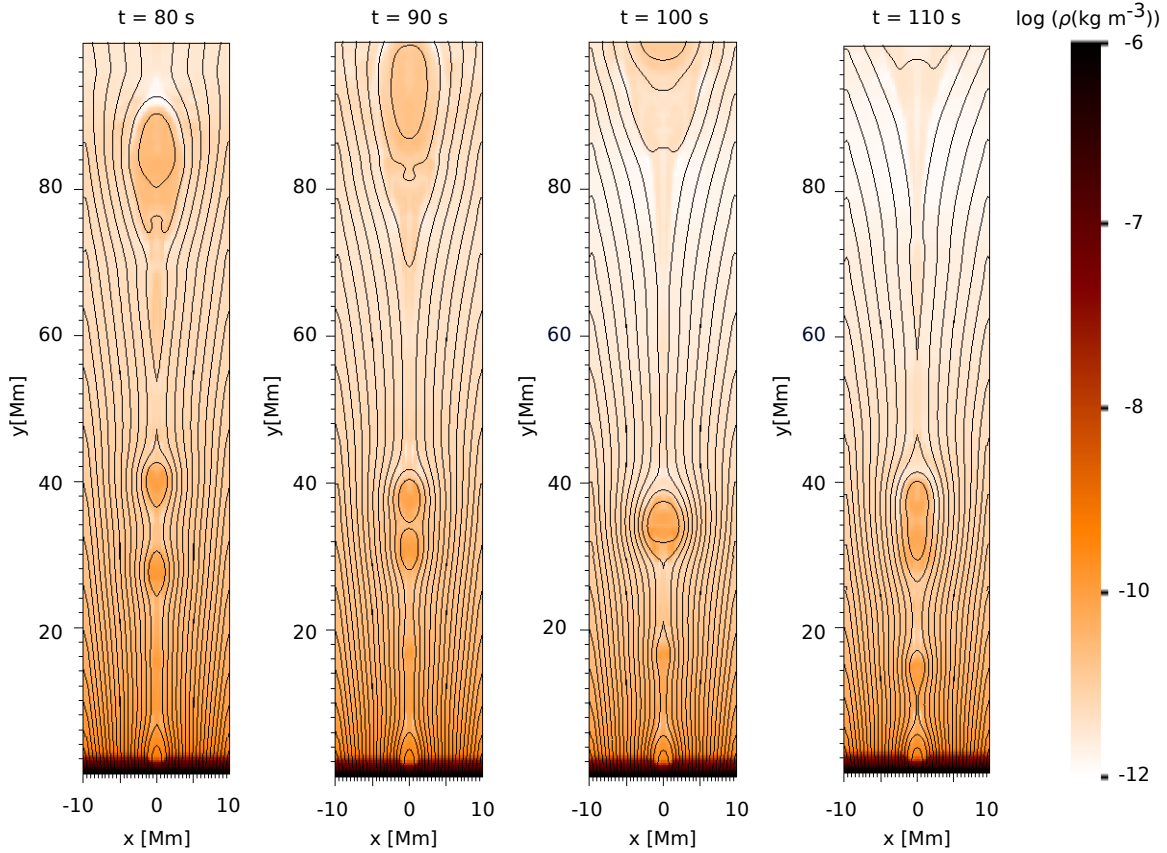


Fig. 2.— The mass density and corresponding magnetic field lines, illustrating the merging of two plasmoids followed by an oscillation of the resulting plasmoid (see the processes in the $y = 20 - 50$ Mm interval). The panels from left to right show times $t = 80, 90, 100$ and 110 s, respectively.

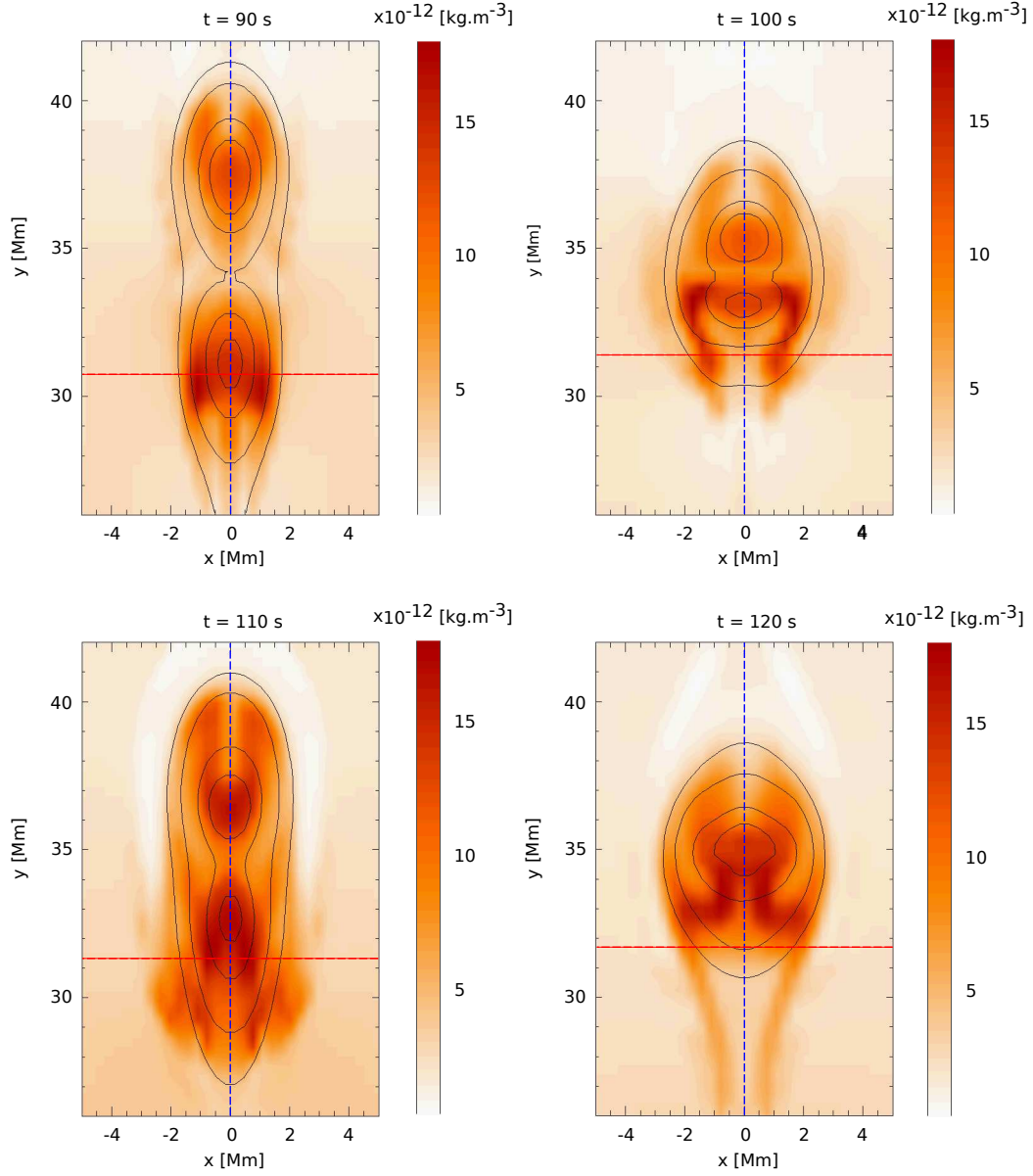


Fig. 3.— A detailed view of the mass density and magnetic field lines of the coalescing plasmoids at different times ($t = 90, 100, 110, 120$ s), showing their self-oscillations and complex density structure.

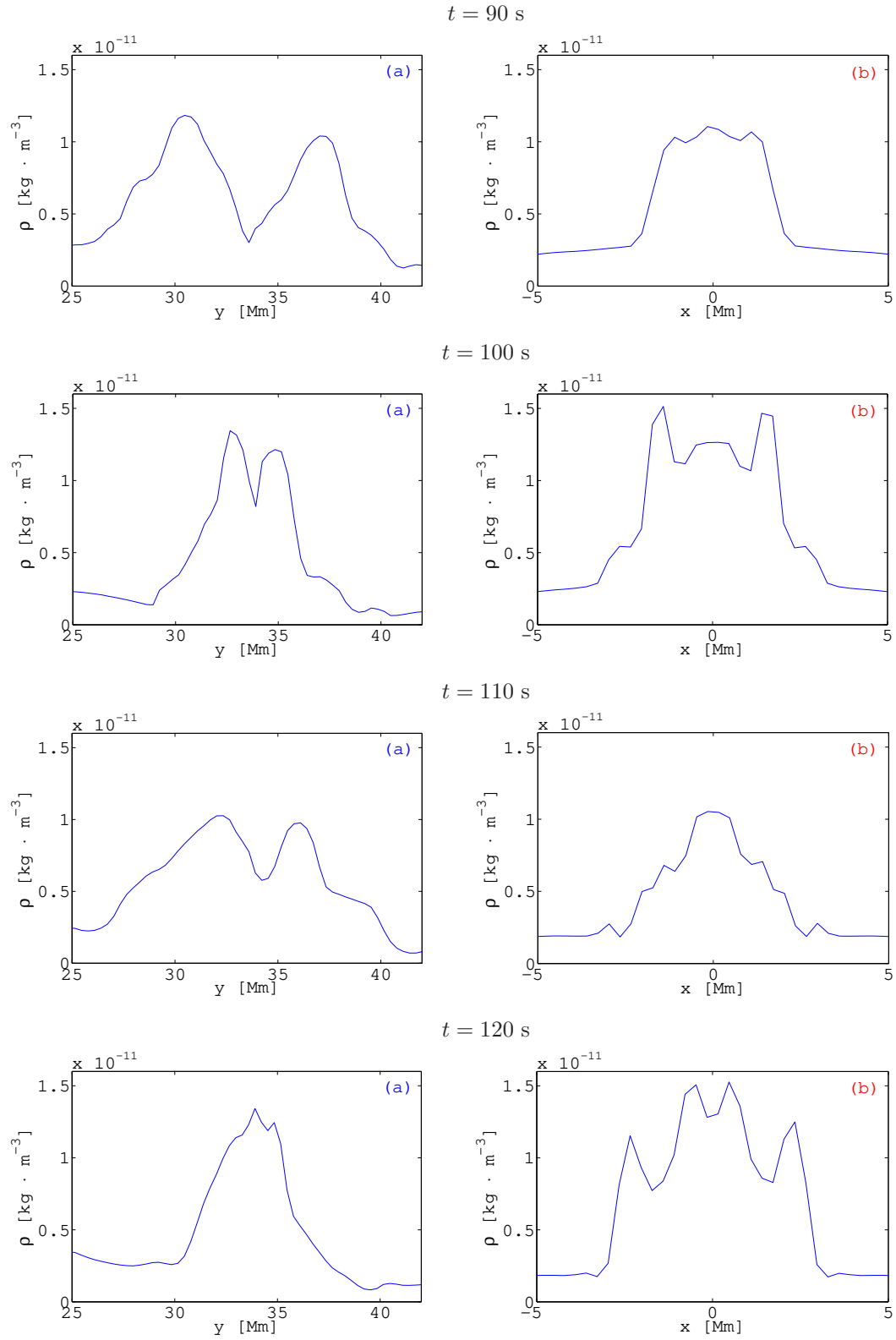


Fig. 4.— Density profiles along the vertical blue (a) and horizontal red (b) lines in Fig. 3.

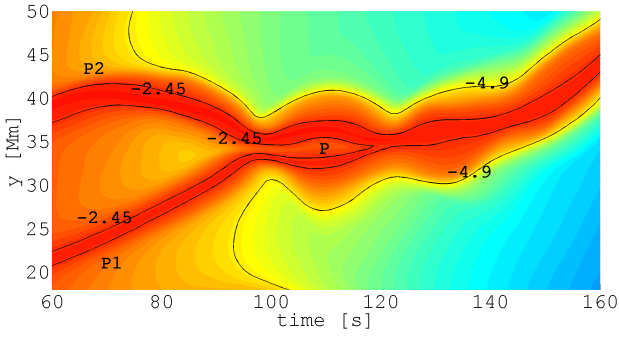


Fig. 5.— The temporal map of the vector potential at heights 18 – 50 Mm above the solar surface. The solid black lines represent the positions of the magnetic field lines with the vector-potential $A = -2.45$ and $A = -4.9$ along the axis of the current sheet during the merging of the two plasmoids (P1 and P2) into one plasmoid (P).

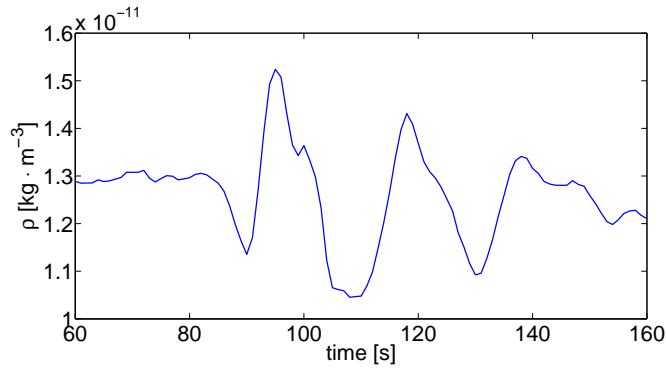


Fig. 6.— The evolution of the maximum mass density in the merging plasmoids, showing periodic behaviour with a period ≈ 25 s.

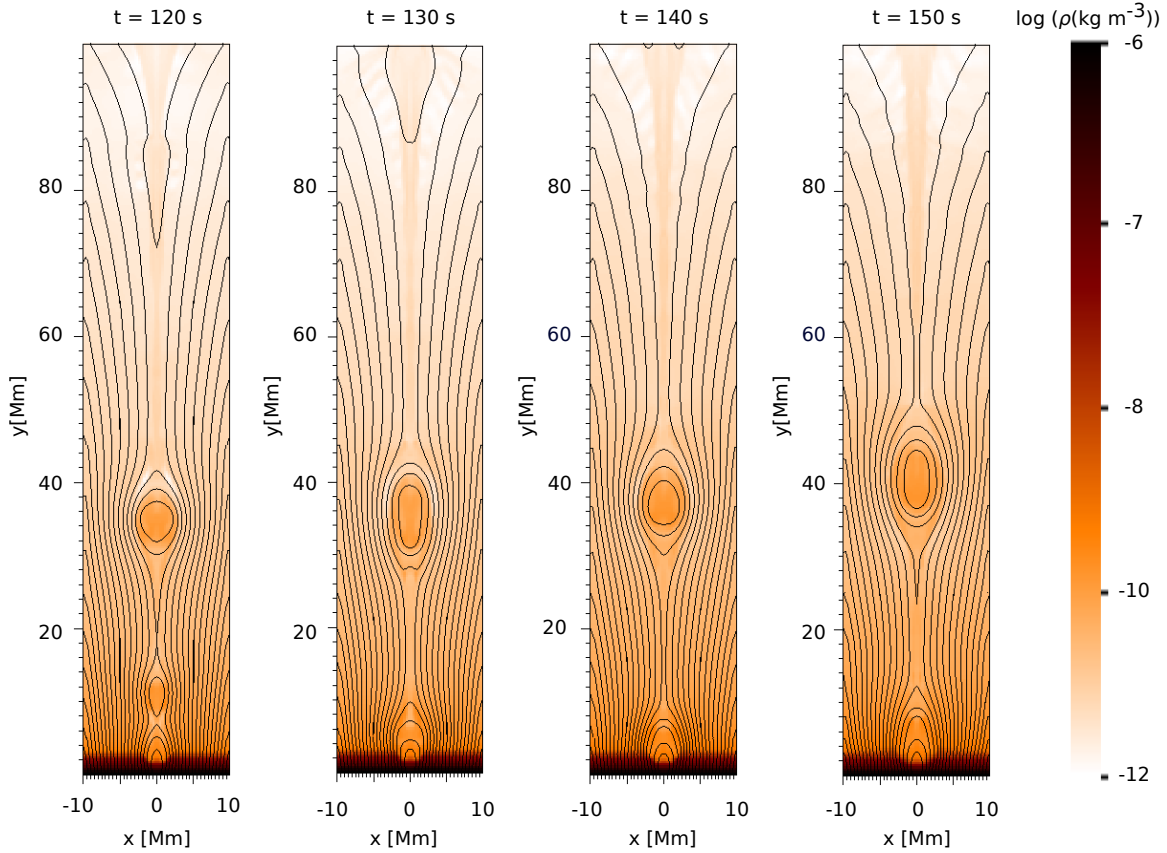


Fig. 7.— The mass density and corresponding magnetic field lines, illustrating the collision of the plasmoid with the magnetic arcade, showing its quickly damped oscillation (see the processes below $y = 20$ Mm). The panels from left to right show times $t = 120, 130, 140$ and 150 s, respectively.

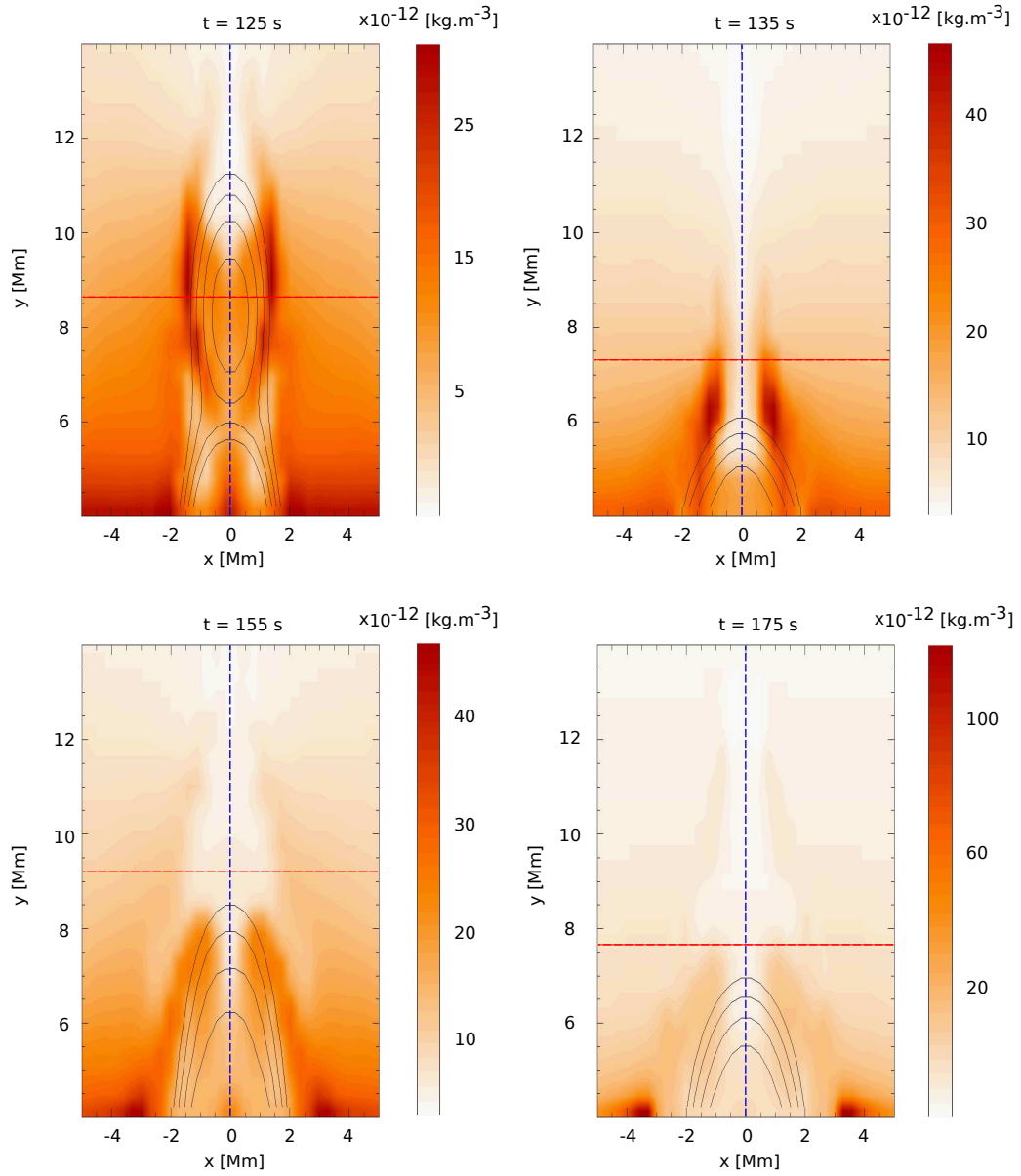


Fig. 8.— A detailed view of densities and magnetic field lines during the merging of the plasmoid with the arcade at times $t = 125, 135, 155, 175 \text{ s}$.

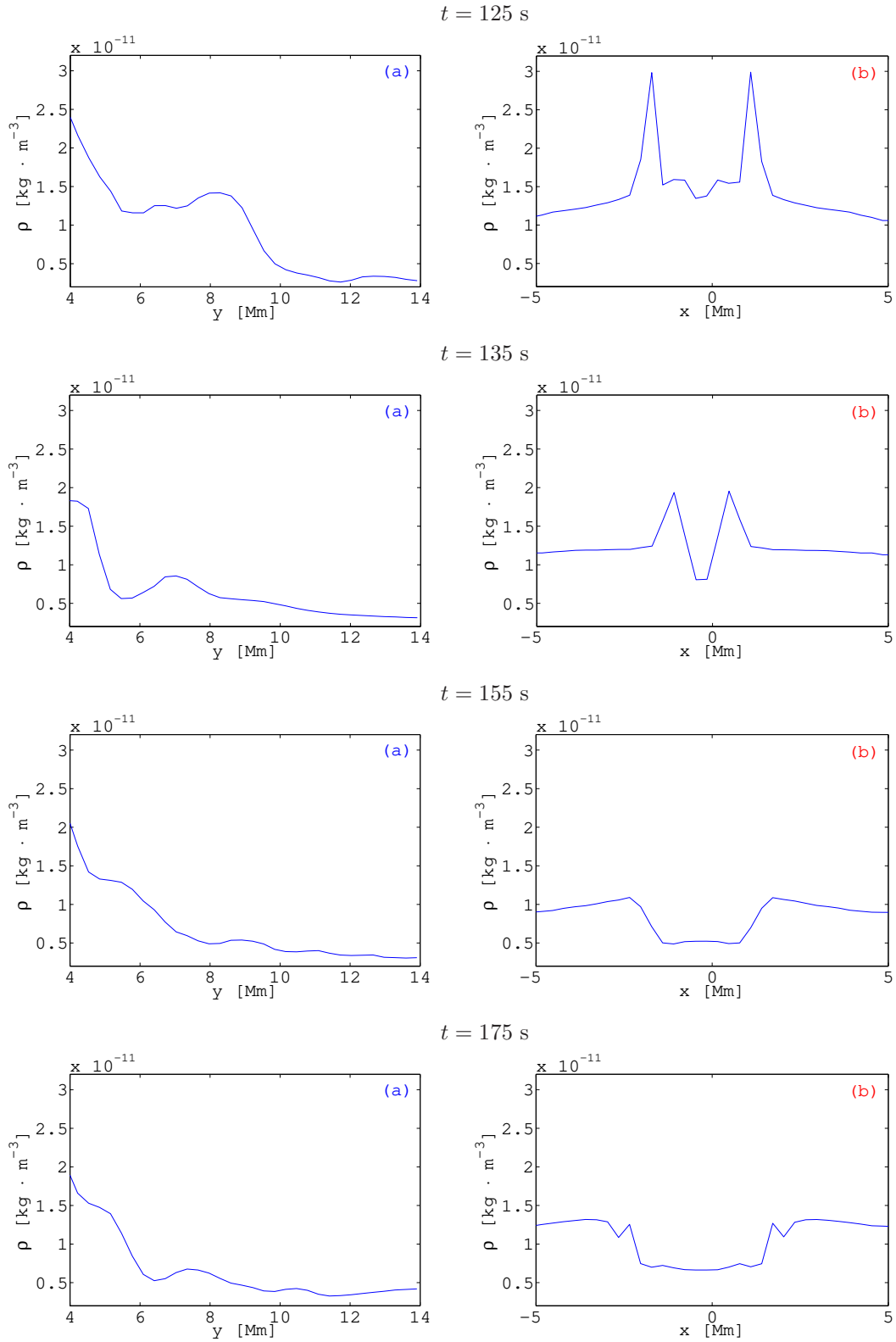


Fig. 9.— Density profiles along the vertical blue (a) and horizontal red (b) lines in Fig. 8.

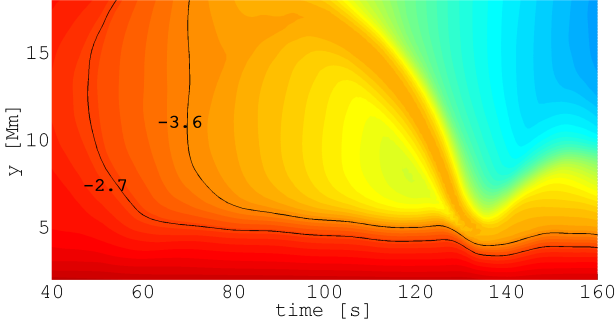


Fig. 10.— The temporal map of the vector potential at heights 2 – 18 Mm above the solar surface. Here we present the evolution of the arcade magnetic field lines having the vector potential $A = -2.7$ and $A = -3.6$, showing its decrease in height in the early phases.

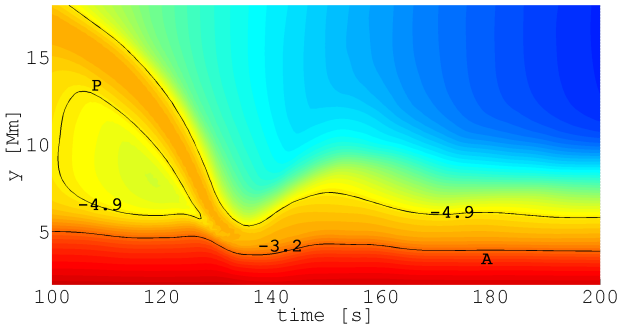


Fig. 11.— The temporal map of the vector potential at heights 2 – 18 Mm above the solar surface. Here we present the evolution of the height of the magnetic field lines at the top of the arcade, corresponding to the vector potential $A = -3.2$ and $A = -4.9$, showing the oscillation of the arcade (A) after its merging with the plasmoid (P).

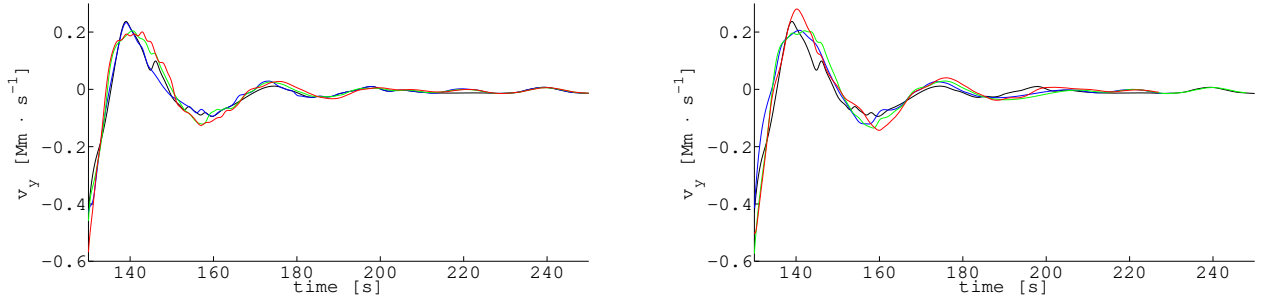


Fig. 12.— Temporal evolution of the y component of the velocity $-v_y$ at the selected magnetic field line with the vector-potential $A = -3.8$, showing the standing waves created after the interaction of the plasmoid with the magnetic arcade. In the left part of the figure the black, blue, green and red lines correspond to the detection positions $x = 0.0; -0.3125; -0.625$ and -0.9375 Mm. On the other hand, in the right part the black, blue, green and red lines correspond to the positions $x = 0.0; +0.3125; +0.625$ and $+0.9375$ Mm. The y coordinates are placed along the selected magnetic field line.

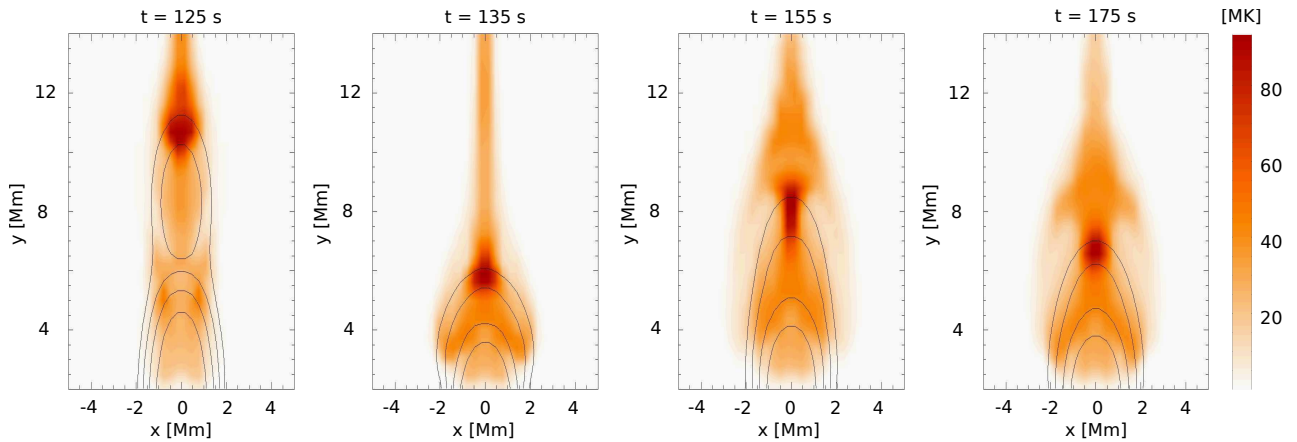
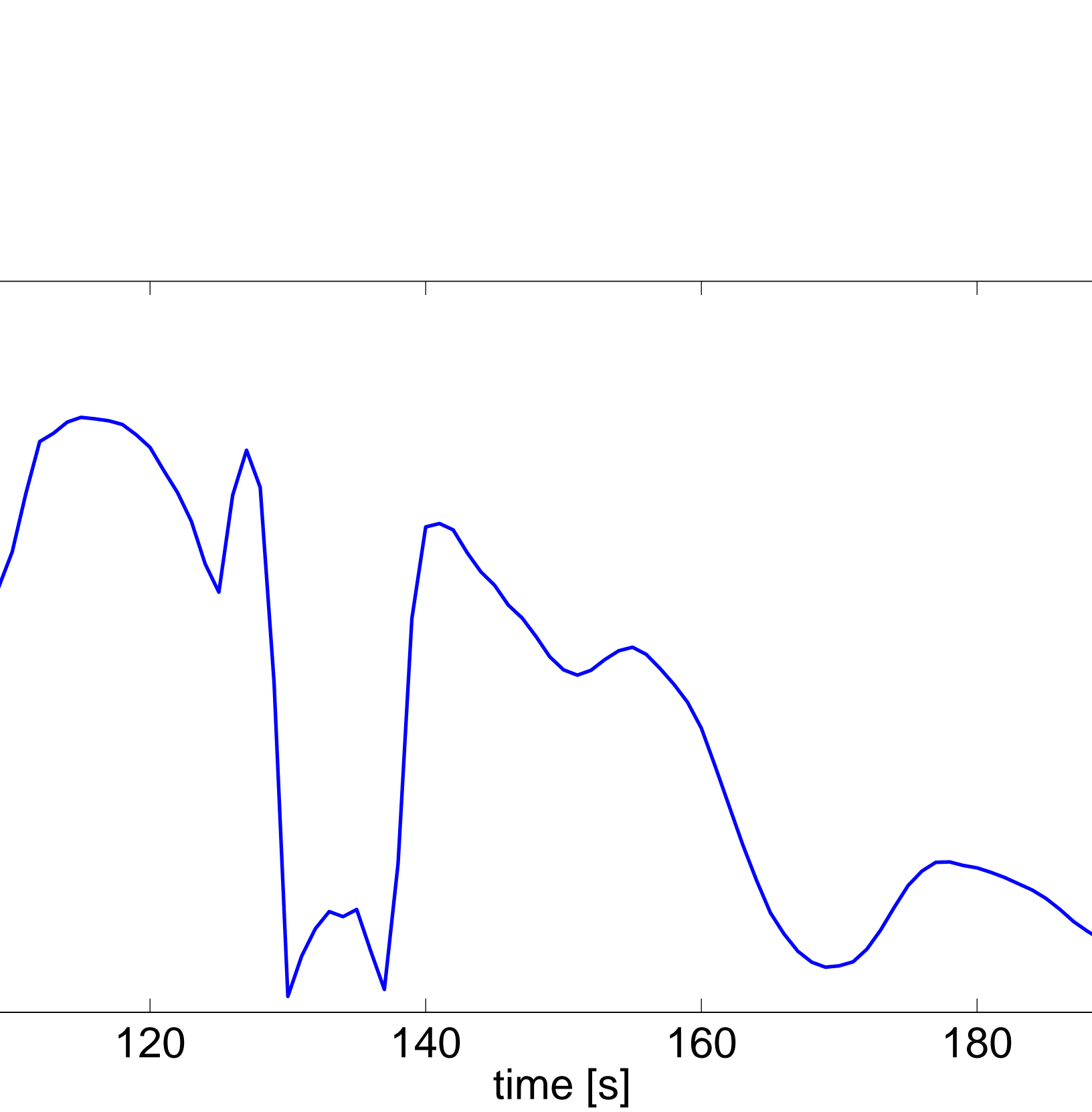
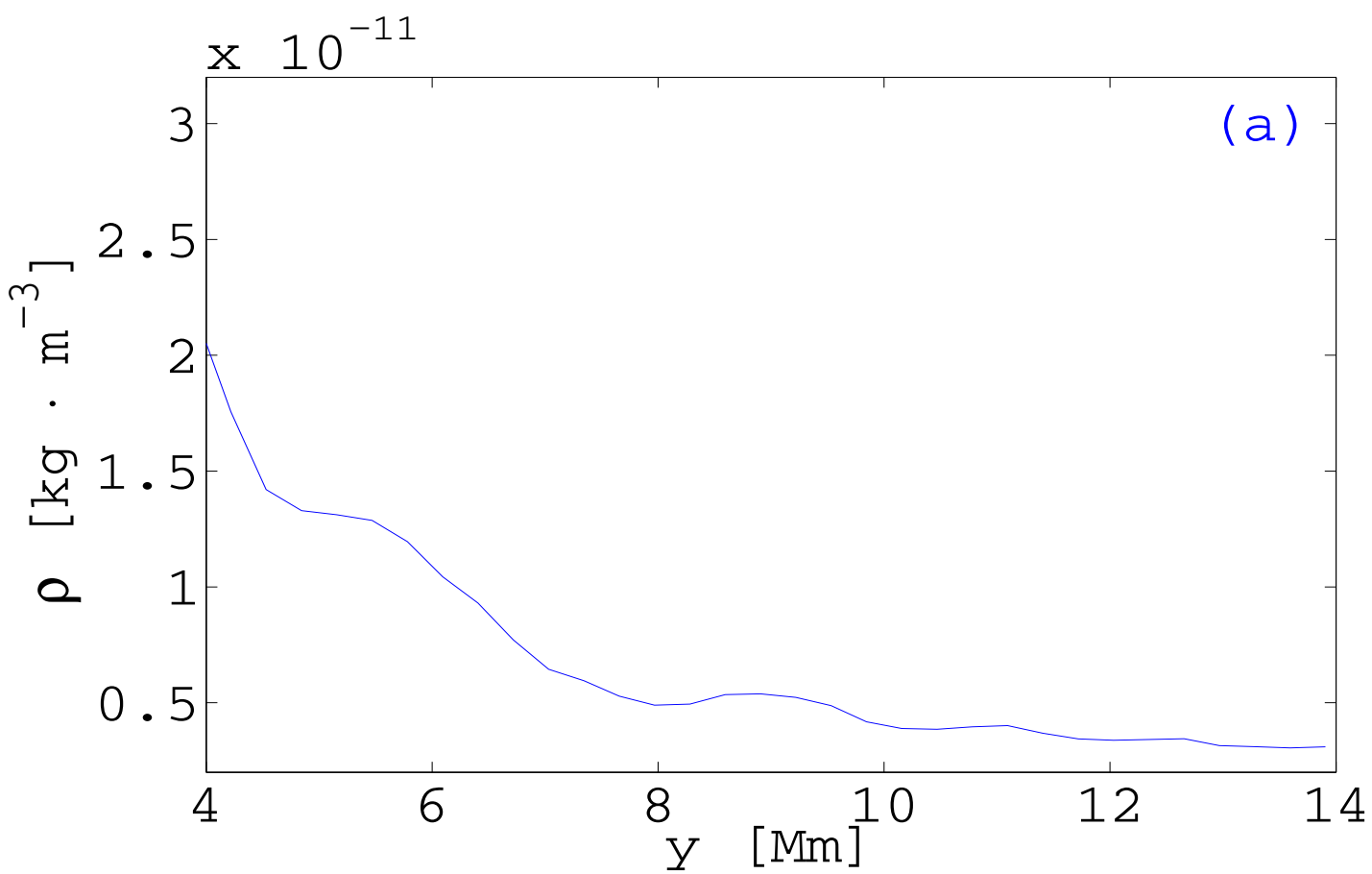


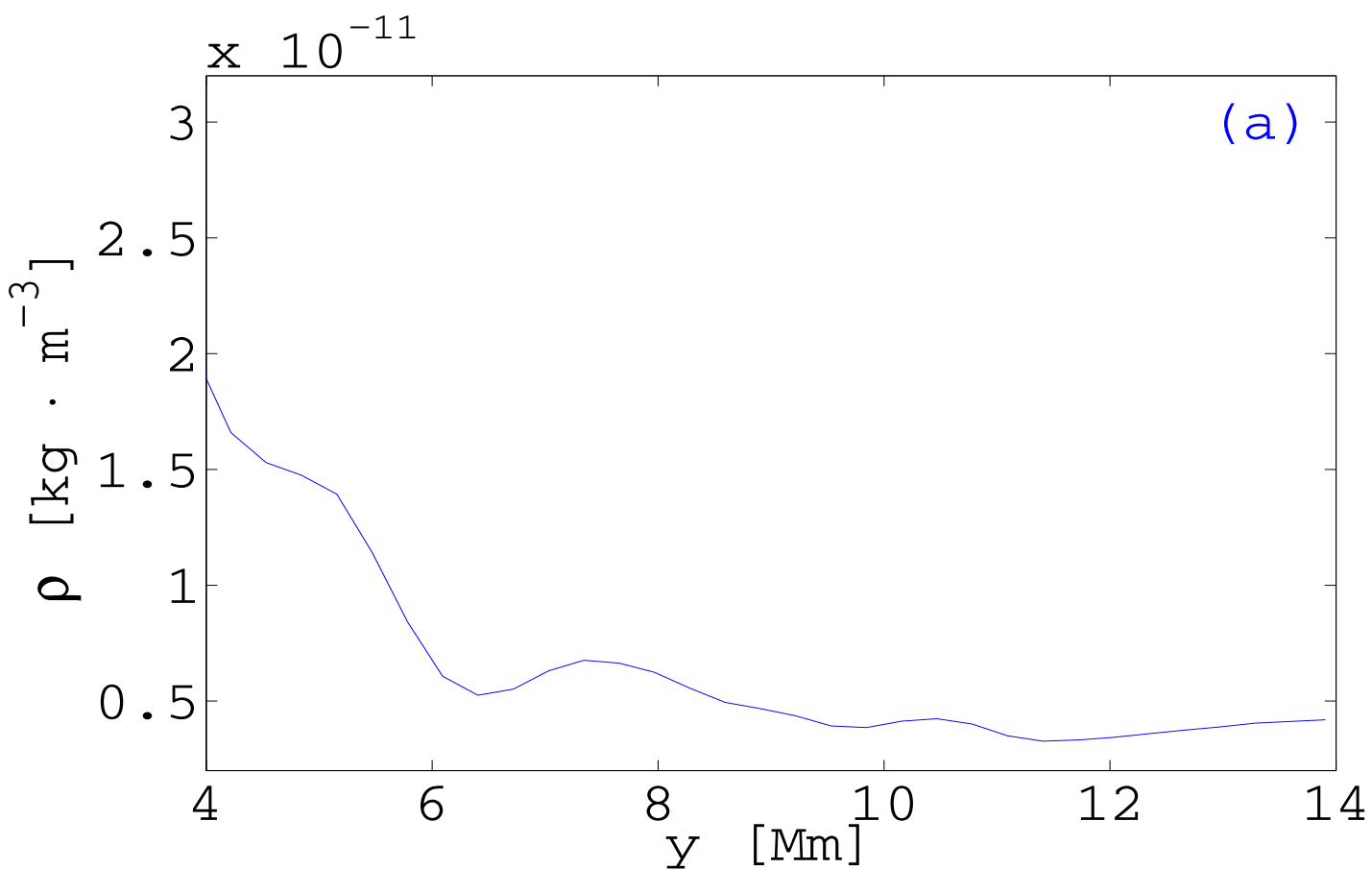
Fig. 13.— The time evolution (for $t = 125, 135, 155, 175$ s) of the temperature in the region of the coalescence of the plasmoid with the magnetic arcade.



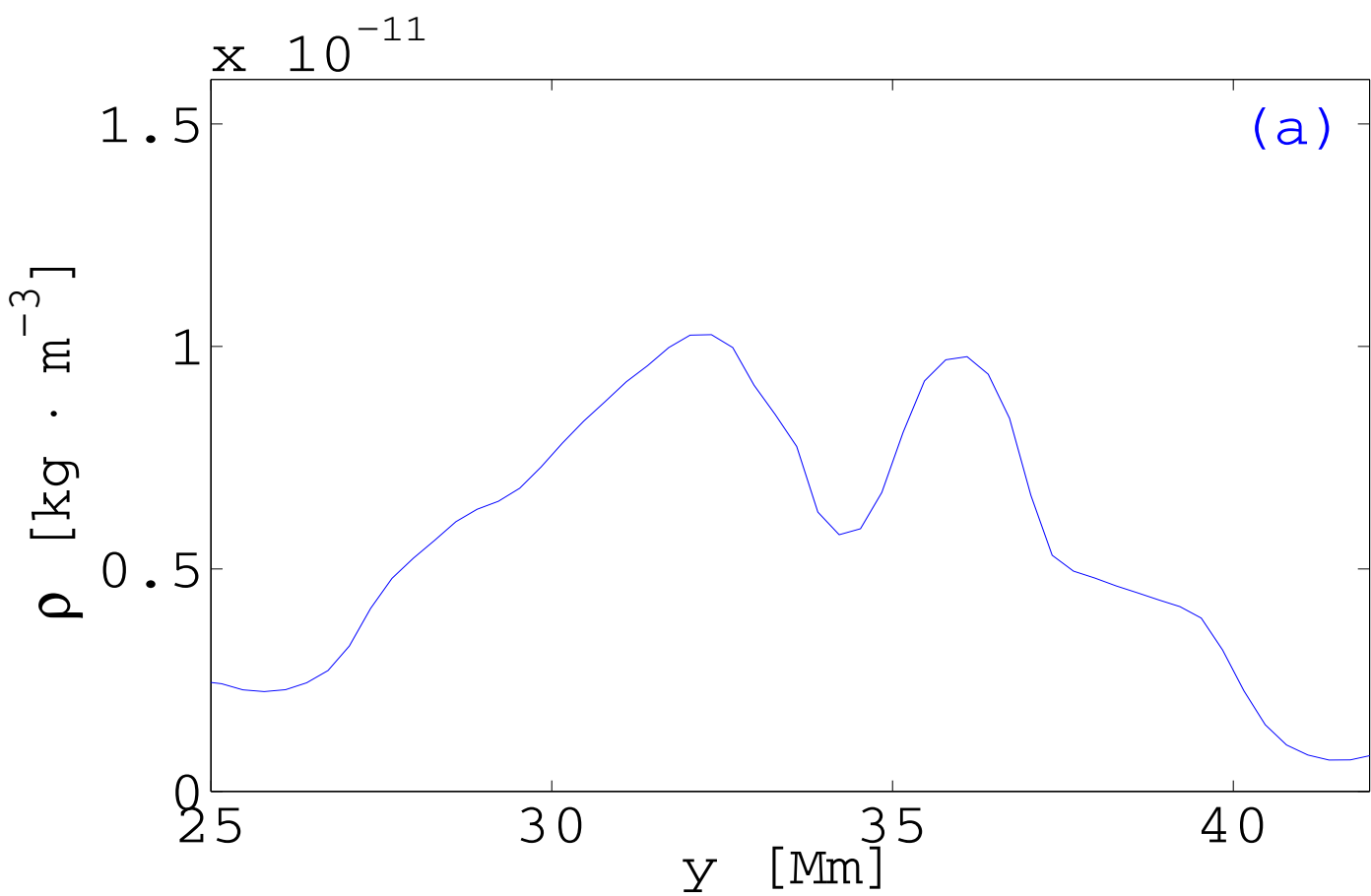
t = 155



t = 175



t = 110



t = 120

